Momentum Analysis for Metasurfaces

Wenwei Liu, Zhancheng Li, Hua Cheng, Shuqi Chen,* and Jianguo Tian
The Key Laboratory of Weak Light Nonlinear Photonics, Ministry of Education, School of Physics and TEDA Institute of Applied Physics, Nankai University, Tianjin 300071, China
(Received 16 January 2017; revised manuscript received 27 April 2017; published 13 July 2017)

Utilizing discrete phase distribution to fit continuous phase distribution has been a primary routine for designing metasurfaces. In the existing method, the validation of the discrete designs is guaranteed only by using the subwavelength condition of unit cells, which is insufficient—especially for arbitrary phase distribution. Herein, we propose an analytical method to design metasurfaces by estimating the width of the source in a unit cell. Also, by calculating field patterns in both real and momentum space, we provide four guidelines for directing future applications of metasurfaces, such as an arbitrary multifocal lens with the same strength of each focus, a convex-concave double lens, and a lens with a large numerical aperture that can precisely prevent undesired diffraction orders. In addition to metalenses, this methodology can provide a wide platform for designing tailored and multifunctional metasurfaces in the future, especially large-area ones in practical applications.

DOI: 10.1103/PhysRevApplied.8.014012

I. INTRODUCTION

Artificially engineered metasurfaces, comprising a dense arrangement of subwavelength resonators, are an efficient and facilely fabricated substitution of bulk metamaterials [1–5]. By introducing an abrupt phase shift to the incident wave front, metasurfaces modify the scattered wave front at deep subwavelength scale, such as anomalous refraction [6,7], metalenses [8–10], holographic plates [11–13], coding metasurfaces [14], wave plates [15], and asymmetric transmission [16–18]. Other alternative applications, including the spin Hall effect [19], topological transitions [20,21], and nonlinear responses [22,23], are also proposed with a specific design of metasurfaces. It has been demonstrated that the generalized refraction is equivalent to blazed diffraction gratings [6,24]. However, the existing quantitative diffracting theories mainly handle either a linearly distributed phase profile or holography, which is highly insufficient compared to the modulation depth of the metasurfaces. In addition, these theories always treat the discontinuous phase distribution as quasicontinuous, which is valid for most of the existing metasurfaces. However, when the phase of each unit cell varies abruptly, or the size of the unit cell is close to or even larger than the wavelength of the signals in nonlinear metasurfaces [22], the hypothesis of quasicontinuous is no longer validated.

Recently, metasurface holography enabling arbitrary wave-front reconstruction and optical communication has attracted considerable research interest in the scientific community [25,26]. Unlike traditional holograms, which are generated by interference of a reference beam with the scattered beam from a real object, the metasurface hologram is generated by numerically computing the phase information at the hologram interface using the computer-generated-holography method [27]. With delicately controlled geometry of the antennas, the desired phase profile can be achieved to accomplish three-dimensional holography [28], surface-plasmon holography [29], multiwavelength achromatic holography [30], and nonlinear holography [31]. Using reflective-type plasmonic metasurfaces [32] and a dielectric Huygens metasurface [33], high-efficiency holograms can also be realized. It is known that holography is based on Fourier analysis to achieve information storage or image reconstruction. Fourier analysis is, indeed, a more fundamental theory that can describe the scattered diffraction field for most of the metasurfaces besides holographic metasurfaces. However, the corresponding analyzing method has not been applied to an arbitrary metasurface, such as metalens.

Moreover, the reflection's law, the regular or generalized Snell's law, and the grating equation are all derived from a single principle: conservation of momentum along the surface of the device (demonstrated in Appendix A). Momentum, which is the wave vector in electrodynamics, and energy are always dominant quantities. Herein, we provide a general guide for evaluating the diffracting field emitted from an arbitrarily arranged metasurface, with tailored functionalities but without considering the specific nanostructures or material details. First, we propose a localized hypothesis of the unit cells composing metasurfaces. The source sizes in the unit cells are considered in comparison with other works, in which the unit cells are characterized simply by a point source with an effective dipole moment [34] or multipolar components [35]. Second, we employ the Fourier analysis to derive a generic

*schen@nankai.edu.cn; http://chenlab.nankai.edu.cn

wave front in k space. We provide four guidelines for designing metasurfaces based on this momentum-analysis method, the most important of which is the stable condition that fulfills the conditions for mimicking continuous phase distribution using a discontinuous phase profile. Taking metalenses as an example, we realize an arbitrary periodic-focus lens, a convex-concave double lens, and a large numerical-aperture (NA) lens preventing undesired diffracting orders via the derived formulas. Our results provide a powerful tool to design the advanced functional and tunable metadevices, especially large-area ones in practical applications.

II. MODELING APPROACH

The strength and phase of output light are two main parameters that facilitate the design of tailorable metasurfaces. When any two adjacent unit cells are weakly coupling (UCWC), these two parameters can characterize an independent unit cell, regardless of the radiation type of the nanostructure [6–18,28–33,36]. Based on this designing strategy, the responding function of a unit cell can be mathematically defined as a rectangular function $t(x) = |t|\mathrm{rect}(x/T^{\mathrm{MS}})e^{-i\phi}$, where $|t|$ is the responding strength (reflection or transmission) and ϕ is the phase delay of the unit cell. The factor $\mathrm{rect}(x/T^{\mathrm{MS}})$ is the estimation of the locality for the unit cell, where T^{MS} describes an equivalent size that the nanostructure can govern, as illustrated in Fig. 1(a). When the parameter of width T^{MS} is small enough relative to the resonant wavelength, the radiating nanostructure can be treated as a point source. Generally, the actual value of T^{MS} should be decided via the geometry and materials of the nanostructures in a unit cell, and it can be simply estimated by the size of the nanostructure. In Appendix B, we compare our theory to the experimental results in Ref. [6] and the simulated results in Ref. [37], where the T^{MS} is set as the size of the nanostructures. The far-field diffraction pattern is the Fourier transform of the responding function based on the principle of superposition [38]: $\mathcal{F}(k) = [(|t|)/\pi]\{[\sin(kT^{\mathrm{MS}}/2)]/k\}e^{-i\phi}$. When the center of the unit cell is located at an arbitrary location x_i, $t(x)$ can be written as

$$t_i(x) = |t_i|\mathrm{rect}\left(\frac{x - x_i}{T_i^{\mathrm{MS}}}\right)e^{-i\phi_i}. \tag{1}$$

According to the translation formula $\mathcal{F}[f(x - x_0)] = e^{-ikx_0}\mathcal{F}[f(x)]$, the Fourier transform of Eq. (1) is

$$\mathcal{F}_i(k) = \frac{|t_i|}{\pi}\frac{\sin(kT_i^{\mathrm{MS}}/2)}{k}e^{-i(\phi_i + kx_i)}. \tag{2}$$

Equation (2) can be illustrated in a metaunit [Fig. 1(b)]. The radius of the sphere is $[(|t_i|)/\pi]\{[\sin(kT_i^{\mathrm{MS}}/2)]/k\}$, characterizing the promoted responding strength of the unit cell. The polar angle $\phi_i/2$ and the azimuthal angle kx_i are decided by the phase delay and location of the unit cell, respectively. The metaunit describes exactly how each unit cell functions in the total scattered wave front. When $\phi_i + kx_i$ is a constant, as depicted by the red starred line in Fig. 1(b), $\mathcal{F}_i$ remains the same, which implies that all of the units on the line are equivalent to each other despite their differing phase delay and locations. This characteristic can be utilized to achieve phase retardation only by varying the location of a unit cell. It should be noted that $\phi_i + kx_i = C$ also represents the wave front (equiphase surface) of $\mathcal{F}_i$ in k space, the envelope of which is a plane wave. The envelope is $\phi_i + \mathbf{k}\cdot\mathbf{r}_i = C$ for two-dimensional metasurfaces, which remains a plane wave in k space (see Appendix C). Specifically, when the constant C of each unit remains the same, the equation for the neighboring unit cell is $\phi_i' + kx_i' = C$. Thus, we obtain $k = -(\phi_i' - \phi_i)/(x_i' - x_i)$. Considering the $2n\pi$ phase uncertainty, the wave front of $\mathcal{F}_i$ (defined as the localized wave vector) can be expressed as

$$k = -\frac{\Delta\phi_i}{\Delta x_i} + \frac{2n\pi}{\Delta x_i}. \tag{3}$$

When ϕ_i varies linearly with x, Eq. (3) is exactly the generalized Snell's law with a diffracting order of n. Furthermore, for a metasurface possessing finite or infinite unit cells, the total responding functions should be the sum of each cell (see Appendix C):

$$T(\mathbf{r}) = \sum_i |t_i| \prod_{v=x,y} \mathrm{rect}\left(\frac{v - v_i}{T_{vi}^{\mathrm{MS}}}\right)e^{-i\phi_i}, \tag{4}$$

$$\mathcal{F}(\mathbf{k}) = \sum_i \frac{|t_i|}{\pi}e^{-i(\phi_i + \mathbf{k}\cdot\mathbf{r}_i)} \prod_{v=x,y} \frac{\sin(k_v T_{vi}^{\mathrm{MS}}/2)}{k_v}. \tag{5}$$

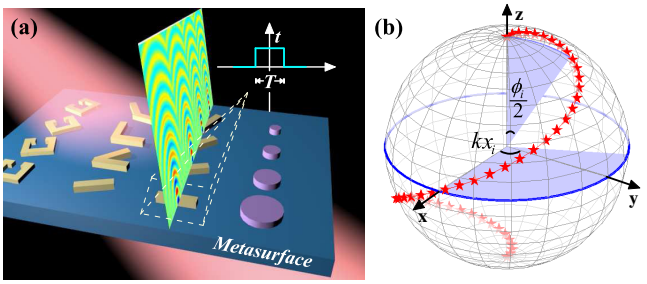

FIG. 1. Localized rectangular model of diffraction theory for metasurfaces. (a) Schematic of an arbitrarily designed metasurface with radiation from every single unit cell. (Inset) Responding function of the ith unit cell with $t = |t_i|e^{-i\phi_i}$ and $T = T_i^{\mathrm{MS}}$. (b) Sphere of the metaunit with polar angle $\phi_i/2$ and azimuthal angle kx_i. The red starred line depicts a class of equivalence with $\phi_i + kx_i = \pi$.

Equations (4) and (5) express the far-field diffraction patterns for all UCWC metasurfaces. Specifically, the diffracting field of a metasurface M_1 with N unit cells is $\mathcal{F}(k) = \sum_{i=1}^{N}[(|t_i|)/\pi]\{[\sin(kT_i^{\mathrm{MS}}/2)]/k\}e^{-i(\phi_i+kx_i)}$. For simplicity, $|t_i| \equiv 1$ and $T_i^{\mathrm{MS}} \equiv T^{\mathrm{MS}} \ll \lambda$ are assumed. Then,

$$\mathcal{F}(k) \propto \mathcal{F}_1(k) \equiv \sum_{i=1}^{N} e^{-i(\phi_i+kx_i)}. \tag{6}$$

Consider another metasurface M_2 with a diffracting field of

$$\mathcal{F}_2(k) \equiv \sum_{i=1}^{N/2} e^{-i(\phi_{2i}+kx_{2i})}. \tag{7}$$

M_2 is obviously composed of all of the even unit cells in M_1. If the diffracting field of M_2 converges, the field should be analogous to the diffracting field of M_1, which implies that

$$\mathcal{F}_2(k) \propto \mathcal{F}_1(k). \tag{8}$$

On the other hand, $\mathcal{F}_1(k)$ and $\mathcal{F}_2(k)$ are related mathematically by

$$\sum_{i=1}^{N} e^{-i(\phi_i+kx_i)} = \sum_{i=1}^{N/2}(1 + e^{i\Delta\phi_{2i}}e^{ik\Delta x_{2i}})e^{-i(\phi_{2i}+kx_{2i})}, \tag{9}$$

where $\Delta\phi_{2i} = \phi_{2i} - \phi_{2i-1}$, $\Delta x_{2i} = x_{2i} - x_{2i-1}$.

Comparing Eqs. (6)–(9), Eq. (8) can be satisfied only when the coefficients of $1 + e^{i\Delta\phi_{2i}}e^{ik\Delta x_{2i}}$ in Eq. (9) are equal to a constant for every i and k. Thus, we attain the conditions for discrete phase distributions to mimic a continuous phase distribution:

$$k\Delta x_{2i} \ll 2\pi, \tag{10}$$

$$\Delta\phi_{2i} \simeq C. \tag{11}$$

Generally, the subscript $2i$ can be replaced by i. Equation (10) is the exact same subwavelength condition, which can be simply written as $\Delta x \ll \lambda$. When the phase of each unit cell varies rapidly, Eq. (11) is nullified, and the subwavelength condition will not guarantee validation of mimicking a continuous phase distribution. Specifically, $\Delta\phi_i \simeq 0$ means that the phase of the unit cell varies slowly. Equation (11) is referred to as the stable condition in this study.

For an arbitrary phase distribution, the following four issues are important.

(1) One-to-one correspondence. Each unit cell produces a plane wave in k space, and each harmonic component in k space corresponds to a unit cell.

(2) Randomness. The entire wave front should be considered since n is any integer in Eq. (3).

(3) Stable condition equation (11). Contrary to the general case, the condition of the subwavelength is not sufficient for mimicking a continuous phase distribution, and the stable condition should also be accomplished.

(4) Evanescent waves. Although $|k| \le k_0$ (the wave vector in free space) should be satisfied for all propagating waves, solutions to Eq. (3) with large values of n must exist due to the principle of the phase uncertainty.

III. APPLICATIONS IN METALENSES

A. Arbitrary multifocal metalenses

The necessity of a stable condition can be interpreted through a metalens. It is well known that a hyperbolic phase profile is equal to a parabolic phase distribution under the paraxial approximation, which is commonly used to simplify the design of a metalens [39]. However, if the phase profile is defined as $\varphi(x) = k_0x^2/2f$, a two-dimensional multifocal metalens can be achieved when x covers a large range, as shown in Fig. 2. The designed metalens has a unit size of 700 nm and focal length of 20 μm operating at a wavelength of 1 μm. Interestingly, the original phase profile and the normalized phase profile are both aperiodic [Fig. 2(a)]; however, the focusing profile is periodic. We design this multifocal lens to demonstrate the stable condition, which differs from the theory in the Ref. [40].

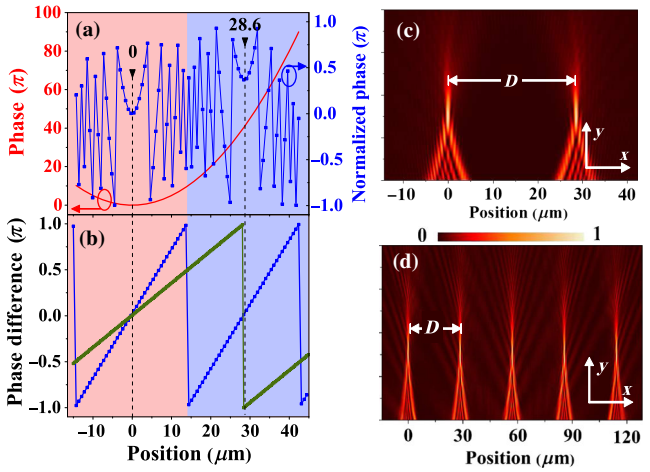

FIG. 2. Multifocal metalens with a lattice size of 700 nm and a focal length of 20 μm, operating at a wavelength of 1 μm. (a) Parabolic phase distribution and its normalized phase distribution of discrete unit cells along the x axis. The red and blue areas indicate different regions of the metalens that serve as independent foci. (b) Phase difference of the adjacent unit cells with a lattice size of 700 nm (the blue dotted line) and 350 nm (the green dotted line). (c) Amplitude distribution of a two-focus metalens. (d) Amplitude distribution of a five-focus metalens.

Evidently, this metalens breaks the stable condition $\Delta\phi_i \simeq C$. As illustrated in Fig. 2(b), the phase difference between two adjacent unit cells varies periodically from $-\pi$ to π, which cannot be considered close to a constant. To theoretically derive this unique phenomenon, let us first consider the phase difference between two adjacent unit cells. Assuming the size of the unit cells is fixed as Λ, the phase difference is $\Delta\varphi(m\Lambda) = \varphi((m+1)\Lambda) - \varphi(m\Lambda) = k_0\Lambda^2(1+2m)/2f$, where m is an integer representing the mth unit cell. Thus, the localized wave vector is $k_m = -\Delta\varphi/\Lambda = -k_0\Lambda(1+2m)/2f$. If the focus of the system is periodic, the localized wave vector should also be periodic. Considering the randomness of the phase, we can obtain the following formula:

$$k_{m+a} = k_m - \frac{2n\pi}{\Lambda}, \tag{12}$$

where a is also an integer representing the number of unit cells for each period. Equation (12) can be precisely solved:

$$a\Lambda = \frac{2n\pi f}{k_0\Lambda}. \tag{13}$$

Thus, when $n = 1$, the minimum period of the foci can be calculated as 28.6 μm from Eq. (13), which is in agreement with the simulated results in Fig. 2(c). Another interesting phenomenon is that, although the size of the unit cell is less than the wavelength, the diffracting field is much different than that of a continuous phase distribution. According to Eq. (13), even when $\Lambda = \lambda/10$, the period of the foci is $10f$, which still is not converged. Furthermore, Eq. (13) can be reformed as

$$\Lambda\left(\frac{a\Lambda}{f}\right) = n\lambda. \tag{14}$$

Comparing this equation to the grating equation $\Lambda\sin\theta = n\lambda$, the designed multifocal metalens is indeed a beam splitter just like a grating. However, for the gratings, $|\sin\theta| \le 1$ is maintained, whereas, for the metalens, $a\Lambda/f$ can theoretically be arbitrarily designed. The numbers of the foci are linearly proportional to the size of the metalens according to Eq. (13). A five-focus metalens is shown in Fig. 2(d), with the same focal distance of 28.6 μm. It should be noticed that the amplitudes of the foci are equal due to the periodicity of the localized wave vector originating from the phase gradient of the metalens. The metalens can serve as a generalized grating with the same strength for all of the diffracting orders.

B. Convex-concave double lens

We also use the proposed theory to design a convex-concave double lens. The unit cells of the metasurface

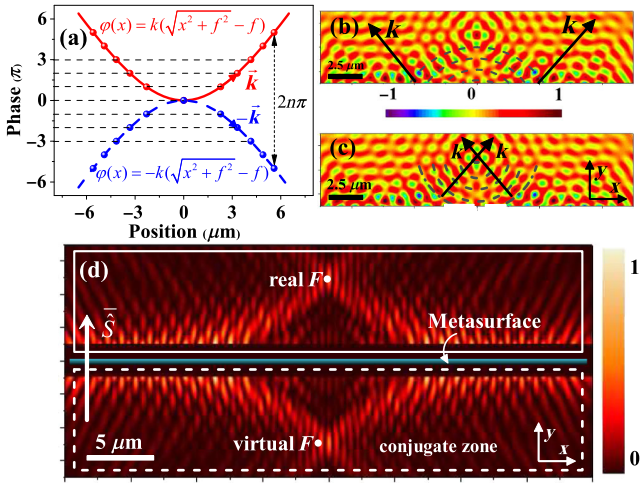

FIG. 3. Designed convex-concave double lens with a focal length of 5 μm operating at a wavelength of 1 μm. (a) Phase distribution along the x axis (the red dots) and its image phase distribution (the blue dots). Locations of the integral π are picked up to locate the unit cells of the lens. (b)–(c) Transmitted field profile of the diverged and focused wave fronts. (d) Strength distribution of the transmitted field (the white solid box) and the effective incident field (the white dashed box). The real and virtual foci are both depicted.

are located at a hyperbolic phase distribution $\varphi(x) = k_0(\sqrt{x^2+f^2} - f) = n\pi$ $(n \in \mathbb{N})$, as indicated by the red dots in Fig. 3(a). It is obvious that these units can generate a focused wave front [Fig. 3(c)]. However, due to the randomness of the phase, the phase profile can also be projected onto another function $\varphi(x) = -k_0(\sqrt{x^2+f^2} - f) = -n\pi$ $(n \in \mathbb{N})$, which can simultaneously achieve a concave lens [Fig. 3(b)]. Similarly, if the blue-dotted phase profile in Fig. 3(a) is first designed, the red-dotted one will occur as well. The one-to-one mapping conjugate phase configuration indicates that this device can converge or diverge an incident photon with the same probability. As shown in Fig. 3(d), the amplitudes of real and virtual F's are both 0.55, according to the simulation, which implies that convex and concave equally serve the functionality of the device. The transmitted field in the white solid box in Fig. 3(d) is totally mirror symmetric to the conjugate zone, and this is a direct consequence of the one-to-one mapping conjugate phase configuration.

To further examine the exact diffraction patterns of the output field, we calculate the $\mathcal{F}$ parameters in Eq. (5) for the regular-focusing metalens, the regular-diverging metalens, and the convex-concave double lens, respectively. In Fig. 4, the horizontal ordinate of the graph is calculated through $\theta = \arcsin(k/k_0)$, characterizing the divergent angle of the output light. The sharp peaks appearing in the lines are caused by the interference of the scattered field, which cannot be eliminated even after improving the calculating accuracy. Interestingly, one cannot recognize a

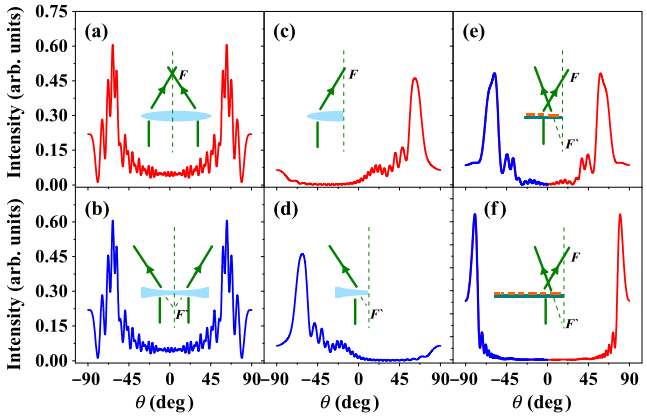

FIG. 4. Calculated $\mathcal{F}$ parameters for (a) the focusing metalens, (b) the diverging metalens, (c) the left side of the focusing metalens, (d) the left side of the diverging metalens, (e) the left side of the convex-concave double lens with 20 unit cells, and (f) the left side of the convex-concave double lens with 100 unit cells. (Insets) Schematics of all of the abovementioned devices. The metalenses in (a)–(d) are designed with a unit size of 500 nm and a focal length of 5 μm operating at a wavelength of 1 μm.

convex or concave lens from a long distance because a parallel incident light diverges after passing the focus of the lens. As shown in Figs. 4(a) and 4(b), the $\mathcal{F}$ parameters are the same for convex and concave metalenses. To distinguish the two lenses, we analyze only the left sides of the devices [Figs. 4(c) and 4(d)]. For a left-sided convex metalens (30 unit cells utilized), the transmitted light travels toward the right side ($\theta \geq 0$), whereas, for a left-sided concave metalens, the transmitted light travels toward the left side ($\theta \leq 0$). By contrast, $\mathcal{F}$ parameters for the left-sided convex-concave double lens are calculated in Fig. 4(e), which combines Figs. 4(c) and 4(d), demonstrating that it can simultaneously work as a convex lens and a concave lens. The minor differences between Figs. 4(c)–4(d) and Fig. 4(e) can be attributed to other orders of diffraction, which primarily exist when $|x|$ and n are small. For example, with $x_1 = 0 (n = 0)$ and $x_2 = -2.29$ μm $(n = 1)$, $-\nabla\varphi_0 = 0.22k_0$ can be obtained. Meanwhile, other phase gradients $-\nabla\varphi_n = -(\Delta\varphi + 2m\pi)/\Delta x = \{-0.22k_0, 0.66k_0, -0.66k_0\}$ are permitted due to phase randomness. On the contrary, when $|x|$ or n is large enough, Δx can be less than a wavelength and $|2m\pi/\Delta x| > k_0$ is maintained for most integers m. In this situation, only the diffracting order of the convex and concave lens can be satisfied, and the efficiency of each component can approach approximately 0.5. The numbers of unit cells are not important for evaluating the functionality of the devices, though they can decide the peak position of the $\mathcal{F}$ parameters. The divergent angle increases as the distance from the center of a lens increases. Thus, the $\mathcal{F}$ parameters of an infinite lens should possess two large peaks around 90° and −90°. In Fig. 4(f), the $\mathcal{F}$ parameters of the convex-concave double lens with 100 unit cells are calculated, which is in complete agreement with the intuitional expects. For all of the calculations in Fig. 4, we assume T^{MS} to be 300 nm around $\lambda/3$. Results for different T^{MS} values are also displayed in Fig. 9 in Appendix E.

C. Large-NA metalens

For the subwavelength hyperbolic metalens, a momentum analysis is also necessary, especially when the NA is large. Considering a phase profile $\varphi(m\Lambda) = k_0[\sqrt{(m\Lambda)^2 + f^2} - f]$, where Λ is the size of the unit cell. We can calculate the phase difference between two adjacent unit cells by $\Delta\varphi(m\Lambda) = k_0[\sqrt{(m\Lambda + \Lambda)^2 + f^2} - \sqrt{(m\Lambda)^2 + f^2}]$. When m is large, $\Delta\varphi(m\Lambda)$ has a limit of $k_0\Lambda$, independent of the focal length f [derived utilizing the Taylor series $(1 + x)^a \approx 1 + ax$], which implies that the hyperbolic phase distribution satisfies the stable condition. If we define $\beta = \Lambda/\lambda$, then $\Delta\varphi(m\Lambda)$ approaches $2\beta\pi$ if m is large enough. As an example, the phase differences for $\beta = 0.7$ and $\beta = 0.4$ are calculated as shown in Fig. 5(a). The dashed lines, indicating asymptotic ones for the corresponding phase difference, are exactly the same as those of the calculated results with $2\beta\pi$. The localized wave vector can be permitted as propagating waves when it satisfies the condition

$$\left|\frac{k_0\Lambda}{\Lambda} + \frac{2n\pi}{\Lambda}\right| \leq k_0, \tag{15}$$

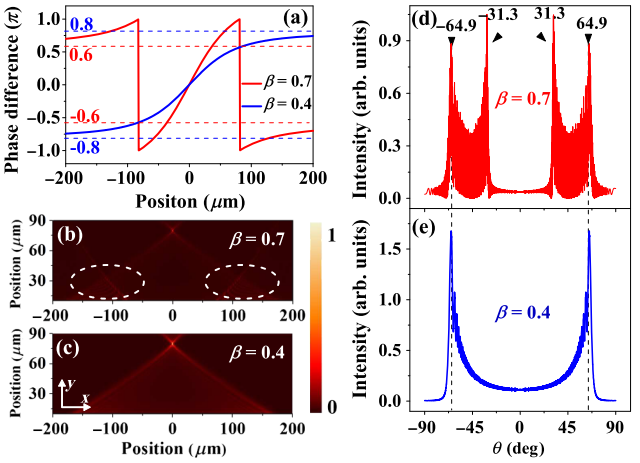

FIG. 5. A hyperbolic metalens with a large NA computed as 0.97 (the total size of the lens is 700 μm). The focal length is 80 μm, operating at a wavelength of 1 μm. The size of the unit cells is set to be $\beta\lambda$. (a) Normalized phase difference between two adjacent unit cells with $\beta = 0.7$ (the red solid line) and $\beta = 0.4$ (the blue solid line). The dashed lines are asymptotic ones for the corresponding phase differences, on which asymptotic values are marked. (b) Simulated focusing field with $\beta = 0.7$. The white dashed circles indicate zones of high-order diffraction. (c) Simulated focusing field with $\beta = 0.4$ without high-order diffractions. Computed $\mathcal{F}$ parameters for (d) $\beta = 0.7$ and (e) $\beta = 0.4$.

which leads to

$$\left|1+\frac{n}{\beta}\right| \leq 1. \tag{16}$$

Considering that the subwavelength condition $0 < \beta < 1$ is often required, the solution of Eq. (16) is $\{n = 0, 0 \leq \beta < 1\}$, or $\{n = -1, 0.5 \leq \beta < 1\}$. When the NA of the metalens is large enough and $0.5 \leq \beta < 1$, the diffracting order of -1 will occur. As indicated by the white-dashed circles in Fig. 5(b), an obvious diffraction occurs when $|x| \geq 70$ μm in the case of $\beta = 0.7$. By contrast, in the case of $\beta = 0.4$, the high orders of diffraction are suppressed to near-field evanescent components, and only a focusing wave front is permitted. An accurate method for evaluating diffraction is to calculate the $\mathcal{F}$ parameters as shown in Figs. 5(d) and 5(e). We can see that the $\mathcal{F}$ parameter for $\beta = 0.7$ has more peaks (diffracting wave vectors) around $\pm 31.3°$. However, the calculated $\mathcal{F}$ parameter for $\beta = 0.4$ is more smooth and has only two main peaks, at around $\pm 64.9°$, which overlap with the corresponding peaks only for $\beta = 0.7$.

IV. CONCLUSION

In this paper, we deduce an enhanced diffraction theory to evaluate the far field for an arbitrary UCWC metasurface, which is based on estimating the width of the source in a unit cell and performing a Fourier transform of the unit cell's responding function. We propose four guidelines to design metasurfaces, especially when the subwavelength condition is no longer sufficient to fit a continuous phase distribution. According to the guidelines, the theory has been employed in applications such as (I) an arbitrary multifocal lens, (II) a convex-concave double lens, and (III) a lens with a large NA preventing undesired diffraction orders. From the theoretical prediction as well as the computational results, the diffracting approach extended to arbitrary phase distributions is demonstrated to be a powerful tool for guiding the design of multifunctional metasurfaces. Our approach provides a wide platform for designing tailored multifunctional, tunable, and, especially, large-area metasurfaces in practical applications.

ACKNOWLEDGMENTS

This work was supported by the National Key Research and Development Program of China (Grant No. 2016YFA0301102), the Natural Science Foundation of China (Grants No. 11574163 and No. 61378006), the Program for New Century Excellent Talents in University (Grant No. NCET-13-0294), and the 111 project (Grant No. B07013). We also acknowledge support from the Collaborative Innovation Center of Extreme Optics, Shanxi University.

APPENDIX A: CONSERVATION OF MOMENTUM FOR BASIC OPTICAL ELEMENTS

In quantum optics, momentum of a photon is linearly related to wave vector: $\mathbf{p} = \hbar\mathbf{k}$. Thus, conservation of momentum also means conservation of wave vectors. The law of reflection states that $\theta_r = \theta_i$, which can also be written as

$$k_0 \sin\theta_r = k_0 \sin\theta_i \Leftrightarrow k_{\|r} = k_{\|i}. \tag{A1}$$

The law of refraction states that $n_t \sin\theta_t = n_i \sin\theta_i$, which also implies

$$k_{\|t} = k_{\|i}. \tag{A2}$$

The generalized Snell's law states that $n_t \sin\theta_t - n_i \sin\theta_i = (\lambda d\Phi)/-(2\pi dx)$ [6], and it can be rewritten as

$$k_{\|t} - k_{\|i} = k_\Lambda, \tag{A3}$$

where $k_\Lambda = d\Phi/dx$ is the phase gradient along the surface of the metasurface.

The equation of gratings is $d(\sin\theta_i + \sin\theta_m) = m\lambda$, which can also be written as

$$k_{\|i} + k_{\|t} = mk_d, \tag{A4}$$

where $k_d = 2\pi/d$ is the reciprocal lattice of the grating.

From Eqs. (A1)–(A4), we can see that the law of reflection, the regular or generalized Snell's law, and the equation of gratings all result from a single principle—conservation of wave vectors along the surface of the device—which motivates us to use $\mathcal{F}$ parameters to characterize flat-optical-element metasurfaces.

APPENDIX B: THEORY TEST

We utilize a simple metasurface grating to test our theory. In Figs. 6(a) and 6(b), the metasurface possesses unity transmittance and the same phase delay in each unit cell. The size of a unit cell is set at $\Lambda = 2\lambda$ (λ is the incident wavelength). It is evident that the transmitted light can be scattered to higher orders of diffraction, $\{0, \pm[(2\pi)/\Lambda], \pm[(4\pi)/\Lambda], \ldots\}$, corresponding to diffracting angles of $\{0, \pm 30°, \pm 90°\}$ (higher orders become evanescent waves).

Figures 6(a) and 6(b) depict the exact diffracting orders the metasurface can provide under the responding function (transmission or reflectance) $t_i(x) = \mathrm{rect}[(x - x_i)/T^{\mathrm{MS}}]e^{-i\phi}$. The blue lines correspond to the zeroth-order diffraction, while the red lines indicate first-order diffractions. It can be seen that the width of the source in a unit cell, T^{MS}, mainly affects the relative strength of each diffracting order. In addition, with $T^{\mathrm{MS}} = 300$ nm, the second-order diffraction at nearly $\pm 90°$ occurs, although diffractions beyond $90°$ evanesce and cannot be detected from the far field.

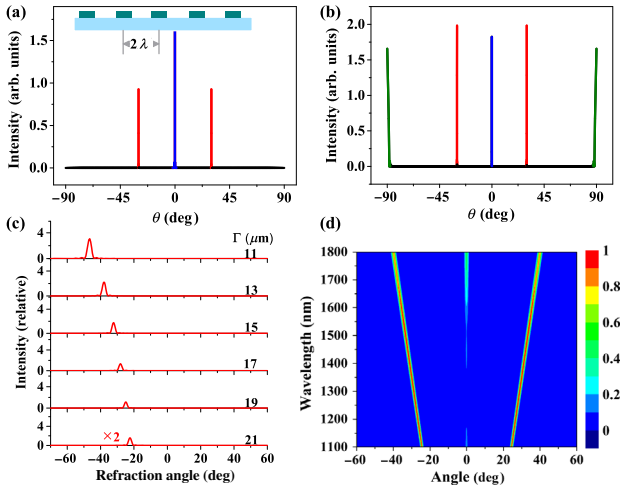

FIG. 6. Computed $\mathcal{F}$ parameters for the metasurface grating with an incident wavelength of 1 μm and unit cell of 2 μm. (a) $T^{\mathrm{MS}} = 900$ nm. (Inset) Schematic of the grating's configuration. (b) $T^{\mathrm{MS}} = 300$ nm. (c) Calculated first-order anomalous refraction based on our theory, for comparison with Fig. 3(c) in Ref. [6]. In the calculation, T^{MS} is set at 1.3 μm (the average size of all of the V-shaped antennas taken from Ref. [6]). (d) Calculated scattered intensity based on our model, for comparison with Fig. 1(c) in Ref. [37]. In the calculation, T^{MS} is set at 1.12 μm (the total size of the three waveguides).

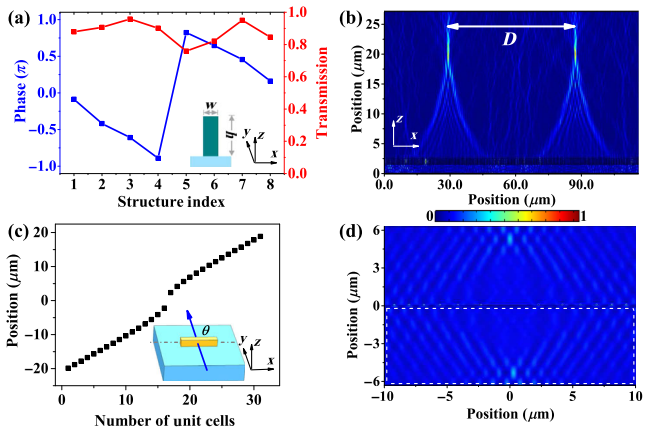

FIG. 7. (a) Phase and transmission of the eight silicon subwavelength structures used in the simulation. (Inset) Schematic dimension of each silicon structure. (b) Simulated two-focus metalens with the structures in (a). (c) Positions of each unit cell used in the simulation to obtain the convex-concave double lens. (Inset) Gold antenna with a length of 230 nm, a width of 40 nm, and a thickness of 40 nm. The orientation angle θ is fixed at 90° to get a Pancharatnam-Berry phase of $2n\pi$. (d) Intensity distribution of the convex-concave double lens.

For a traditional grating, the responding function is an exact rectangular function, while, for an arbitrary metasurface, the factor $\mathrm{rect}(x/T^{\mathrm{MS}})$ is an equivalent estimation of a unit cell's locality.

To test our theoretical model, we compare the experimental results in Ref. [6] to our calculated model. In our calculation, T^{MS} is set as 1.3 μm by averaging four basic V-shaped antennas in Ref. [6]. The total size of the metasurface in the calculation is 230 μm. The phase and the intensity of each antenna are taken from the reference. Specifically, besides the refraction angle, the height and the width of the peaks in Fig. 6(c) coincide with those in Fig. 3(c) from Ref. [6]. We also compare the simulated results in Ref. [37] to our calculated model, as shown in Fig. 6(d). The main peaks of the scattered intensity are in agreement with the results in Ref. [37], and the relative intensity also makes sense. The width of the diffraction peaks in periodic structures is determined by the total number of unit cells, which is not mentioned in Ref. [37]. Therefore, we did not compare the width of these peaks to the results in Ref. [37].

The designed metasurfaces in the main text can be easily achieved. As an example, we use a two-dimensional simulation with a dielectric metasurface to acquire a result similar to that of Fig. 2(c), as shown in Figs. 7(a) and 7(b). The lattice size of the metasurface is 450 nm, with a focal length of 20 μm, operating at a wavelength of 1310 nm; the incident light is polarized along the y direction. The height of the silicon structure is 1033 nm, and the widths w of the silicon are 95, 120, 135, 160, 205, 250, 300, and 390 nm, respectively. The refraction index of silicon is set at 3.45. The simulated distance between the two foci is $D = 58.22$ μm, and the calculated distance according to Eq. (13) is 58.22 μm as well. We also use a plasmonic metasurface to achieve the convex-concave double lens. The positions of each gold antenna are depicted in Fig. 7(c), and the intensity distribution in Fig. 7(d) is consistent with that in Fig. 3(d).

APPENDIX C: $\mathcal{F}$ PARAMETERS FOR A TWO-DIMENSIONAL METASURFACE

The responding function of the ith unit cell located at (x_i, y_i) can be written as

$$T_i(x,y) = |t_i|\mathrm{rect}\left(\frac{x-x_i}{T_{xi}^{\mathrm{MS}}}\right)\mathrm{rect}\left(\frac{y-y_i}{T_{yi}^{\mathrm{MS}}}\right)e^{-i\phi_i}. \quad \text{(C1)}$$

By performing a two-dimensional Fourier transform, the diffracting field in k space is

$$\mathcal{F}_i(k_x,k_y) = \frac{|t_i|}{\pi}e^{-i(\phi_i+k_x x_i+k_y y_i)} \times \frac{\sin(k_x T_{xi}^{\mathrm{MS}}/2)}{k_x}\frac{\sin(k_y T_{yi}^{\mathrm{MS}}/2)}{k_y}. \quad \text{(C2)}$$

Thus, the total responding function and diffraction pattern should be

$$T(\mathbf{r}) = \sum_i |t_i| \prod_{v=x,y} \mathrm{rect}\left(\frac{v - v_i}{T_{vi}^{\mathrm{MS}}}\right) e^{-i\phi_i}, \tag{C3}$$

$$\mathcal{F}(\mathbf{k}) = \sum_i \frac{|t_i|}{\pi} e^{-i(\phi_i + \mathbf{k}\cdot\mathbf{r}_i)} \prod_{v=x,y} \frac{\sin(k_v T_{vi}^{\mathrm{MS}}/2)}{k_v}. \tag{C4}$$

APPENDIX D: CALCULATING METHODS

The field profiles in Figs. 2(c), 2(d), 3(b)–3(d), 5(b), and 5(c) in the main text are calculated with the commercial software MATLAB, with each unit cell of the metasurface regarded as a secondary source that can radiate a spherical wave. Based on theoretical and experimental research from other groups [6–18,28–33,36], the main properties of a metasurface are decided by the strength of the output light and the phase of each unit cell, despite the unit cell's radiating type. Thus, we use a spherical wave as a secondary source to test the validity of the field profile.

Specifically, the conjugate zone in Fig. 3(d) is computed through deduction as follows.

The wave front is the contour map of the wave's phase, and the wave vector is the gradient vector of this map, written as $\mathbf{k} = -\nabla\varphi$. Thus, the wave will propagate along $\mathbf{k}$. If we want to recover the incident wave, we can just reverse the direction of $\mathbf{k}$ such that $-\mathbf{k} = \nabla\varphi = -\nabla(-\varphi)$. As shown in Fig. 8(a), a plane wave is generated by a metasurface with a phase distribution of $-0.3k_0r$ located along $y = 0$. The wave propagates at $-17.5°$, as computed with $\arcsin(-0.3) = -17.5°$. Figure 8(b) is computed by reversing the phase distribution as $0.3k_0r$ to rebuild the incident wave.

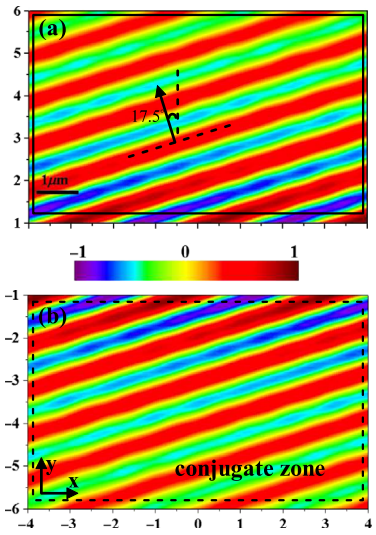

FIG. 8. (a) A propagating plane wave and (b) a rebuilt incident wave depicted by a dashed box.

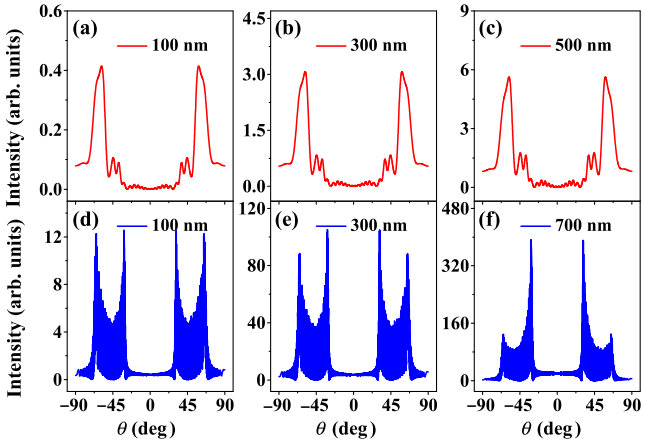

FIG. 9. Calculated $\mathcal{F}$ parameters for the convex-concave double lens designed in Figs. 2 and 3 with (a) $T^{\mathrm{MS}} = 100$ nm, (b) $T^{\mathrm{MS}} = 300$ nm, and (c) $T^{\mathrm{MS}} = 500$ nm. Calculated $\mathcal{F}$ parameters for the metalenses designed in Fig. 5 with (d) $T^{\mathrm{MS}} = 100$ nm, (e) $T^{\mathrm{MS}} = 300$ nm, and (f) $T^{\mathrm{MS}} = 700$ nm.

APPENDIX E: DIFFRACTING PATTERNS WITH DIFFERENT VALUES OF T^{MS}

$\mathcal{F}(k) = \sum_i [(|t_i|)/\pi]\{[\sin(kT_i^{\mathrm{MS}}/2)]/k\}e^{-i(\phi_i + kx_i)}$ degenerates to $\mathcal{F}(k) \approx \sum_i [(T_i^{\mathrm{MS}}|t_i|)/2\pi]e^{-i(\phi_i + kx_i)}$ when the width parameter T^{MS} is sufficiently small and the strength of the $\mathcal{F}$ parameters is approximately proportional to the size of T^{MS}. This also means that when T^{MS} is sufficiently small, the diffracting patterns remain the same, regardless of the value of T^{MS}. However, when T^{MS} is large (still smaller than a wavelength), it affects $\mathcal{F}_i$ as a sine function; the corresponding results can be seen in Figs. 6(a) and 6(b). We also plot different diffracting patterns of the designed convex-concave double lens for different T^{MS}'s, as shown in Figs. 9(a)–9(c). The incident wavelength is 1 μm and the size of the unit cell is 500 nm. All of the values of T^{MS} are chosen to be $T^{\mathrm{MS}} < \Lambda = 500$ nm, and all of the diffracting patterns are almost the same in this case. As for the metalenses designed in Fig. 5, $\mathcal{F}$ parameters differ when the size of T^{MS} varies from 100 to 700 nm, as shown in Figs. 9(d)–9(f). The position of each diffractive peak remains the same, while the amplitude varies for different values of T^{MS}, and this result fits with the diffracting patterns of a metasurface grating, as stated in Appendix B.

[1] S. Wu, Z. Zhang, Y. Zhang, K. Zhang, L. Zhou, X. Zhang, and Y. Zhu, Enhanced Rotation of the Polarization of a Light Beam Transmitted through a Silver Film with an Array of Perforated S-Shaped Holes, Phys. Rev. Lett. **110**, 207401 (2013).

[2] A. E. Minovich, A. E. Miroshnichenko, A. Y. Bykov, T. V. Murzina, D. N. Neshev, and Y. S. Kivshar, Functional and

nonlinear optical metasurfaces, Laser Photonics Rev. **9**, 195 (2015).
[3] A. V. Kildishev, A. Boltasseva, and V. M. Shalaev, Planar photonics with metasurfaces, Science **339**, 1232009 (2013).
[4] H. Cheng, Z. Liu, S. Chen, and J. Tian, Emergent Functionality and Controllability in Few-Layer Metasurfaces, Adv. Mater. **27**, 5410 (2015).
[5] D. Lin, P. Fan, E. Hasman, and M. L. Brongersma, Dielectric gradient metasurface optical elements, Science **345**, 298 (2014).
[6] N. Yu, P. Genevet, M. A. Kats, F. Aieta, J. P. Tetienne, F. Capasso, and Z. Gaburro, Light propagation with phase discontinuities: Generalized laws of reflection and refraction, Science **334**, 333 (2011).
[7] X. Ding, F. Monticone, K. Zhang, L. Zhang, D. Gao, S. N. Burokur, and A. Alù, Ultrathin Pancharatnam-Berry Metasurface with Maximal Cross Polarization Efficiency, Adv. Mater. **27**, 1195 (2015).
[8] X. Ni, S. Ishii, A. V. Kildishev, and V. M. Shalaev, Ultra-thin, planar, Babinet-inverted plasmonic metalenses, Light Sci. Appl. **2**, e72 (2013).
[9] X. Chen, L. Huang, H. Mühlenbernd, G. Li, B. Bai, Q. Tan, G. Jin, C. Qiu, S. Zhang, and T. Zentgraf, Dual-polarity plasmonic metalens for visible light, Nat. Commun. **3**, 1198 (2012).
[10] D. Wintz, P. Genevet, A. Ambrosio, A. Woolf, and F. Capasso, Holographic metalens for switchable focusing of surface plasmons, Nano Lett. **15**, 3585 (2015).
[11] S. Larouche, Y. J. Tsai, T. Tyler, N. M. Jokerst, and D. R. Smith, Infrared metamaterial phase holograms, Nat. Mater. **11**, 450 (2012).
[12] G. Zheng, H. Mühlenbernd, M. Kenney, G. Li, T. Zentgraf, and S. Zhang, Metasurface holograms reaching 80% efficiency, Nat. Nanotechnol. **10**, 308 (2015).
[13] J. Lin, P. Genevet, M. A. Kats, N. Antoniou, and F. Capasso, Nanostructured holograms for broadband manipulation of vector beams, Nano Lett. **13**, 4269 (2013).
[14] L. H. Gao, Q. Cheng, J. Yang, S. J. Ma, J. Zhao, S. Liu, and Q. Y. Wen, Broadband diffusion of terahertz waves by multi-bit coding metasurfaces, Light Sci. Appl. **4**, e324 (2015).
[15] Y. Zhao and A. Alù, Tailoring the dispersion of plasmonic nanorods to realize broadband optical meta-waveplates, Nano Lett. **13**, 1086 (2013).
[16] C. Pfeiffer, C. Zhang, V. Ray, L. J. Guo, and A. Grbic, High Performance Bianisotropic Metasurfaces: Asymmetric Transmission of Light, Phys. Rev. Lett. **113**, 023902 (2014).
[17] J. H. Shi, H. F. Ma, C. Y. Guan, Z. P. Wang, and T. J. Cui, Broadband chirality and asymmetric transmission in ultrathin 90-twisted Babinet-inverted metasurfaces, Phys. Rev. B **89**, 165128 (2014).
[18] C. Menzel, C. Helgert, C. Rockstuhl, E. B. Kley, A. Tünnermann, T. Pertsch, and F. Lederer, Asymmetric Transmission of Linearly Polarized Light at Optical Metamaterials, Phys. Rev. Lett. **104**, 253902 (2010).
[19] X. Yin, Z. Ye, J. Rho, Y. Wang, and X. Zhang, Photonic spin Hall effect at metasurfaces, Science **339**, 1405 (2013).
[20] J. S. Gomez-Diaz, M. Tymchenko, and A. Alù, Hyperbolic Plasmons and Topological Transitions over Uniaxial Metasurfaces, Phys. Rev. Lett. **114**, 233901 (2015).
[21] W. Gao, M. Lawrence, B. Yang, F. Liu, F. Fang, B. Béri, J. Li, and S. Zhang, Topological Photonic Phase in Chiral Hyperbolic Metamaterials, Phys. Rev. Lett. **114**, 037402 (2015).
[22] Y. Yang, W. Wang, A. Boulesbaa, I. I. Kravchenko, D. P. Briggs, A. Puretzky, and J. Valentine, Nonlinear Fano-resonant dielectric metasurfaces, Nano Lett. **15**, 7388 (2015).
[23] M. Tymchenko, J. S. Gomez-Diaz, J. Lee, N. Nookala, M. A. Belkin, and A. Alù, Gradient Nonlinear Pancharatnam-Berry Metasurfaces, Phys. Rev. Lett. **115**, 207403 (2015).
[24] S. Larouche and D. R. Smith, Reconciliation of generalized refraction with diffraction theory, Opt. Lett. **37**, 2391 (2012).
[25] S. Larouche, Y. J. Tsai, T. Tyler, N. M. Jokerst, and D. R. Smith, Infrared metamaterial phase holograms, Nat. Mater. **11**, 450 (2012).
[26] Y. W. Huang, W. T. Chen, W. Y. Tsai, P. C. Wu, C. M. Wang, G. Sun, and D. P. Tsai, Aluminum plasmonic multicolor meta-hologram, Nano Lett. **15**, 3122 (2015).
[27] C. Slinger, C. Cameron, and M. Stanley, Computer-generated holography as a generic display technology, Computer **38**, 46 (2005).
[28] L. Huang, X. Chen, H. Mühlenbernd, H. Zhang, S. Chen, B. Bai, Q. Tan, G. Jin, K. W. Cheah, C. W. Qiu, J. Li, T. Zentgraf, and S. Zhang, Three-dimensional optical holography using a plasmonic metasurface, Nat. Commun. **4**, 2808 (2013).
[29] Q. Xu, X. Zhang, Y. Xu, C. Ouyang, Z. Tian, J. Gu, J. Li, S. Zhang, J. Han, and W. Zhang, Polarization-controlled surface plasmon holography, Laser Photonics Rev. **11**, 1600212 (2017).
[30] B. Wang, F. Dong, Q. T. Li, D. Yang, C. Sun, J. Chen, Z. Song, L. Xu, W. Chu, Y. F. Xiao, Q. Gong, and Y. Li, Visible-frequency dielectric metasurfaces for multiwavelength achromatic and highly dispersive holograms, Nano Lett. **16**, 5235 (2016).
[31] W. Ye, F. Zeuner, X. Li, B. Reineke, S. He, C. W. Qiu, J. Liu, Y. Wang, S. Zhang, and T. Zentgraf, Spin and wavelength multiplexed nonlinear metasurface holography, Nat. Commun. **7**, 11930 (2016).
[32] W. T. Chen, K. Y. Yang, C. M. Wang, Y. W. Huang, G. Sun, I. D. Chiang, C. Y. Liao, W. L. Hsu, H. T. Lin, S. Sun, L. Zhou, A. Q. Liu, and D. P. Tsai, High-efficiency broadband meta-hologram with polarization-controlled dual images, Nano Lett. **14**, 225 (2014).
[33] W. Zhao, H. Jiang, B. Liu, J. Song, Y. Jiang, C. Tang, and J. Li, Dielectric Huygens' Metasurface for High-Efficiency Hologram Operating in Transmission Mode, Sci. Rep. **6**, 30613 (2016).
[34] G. Li, S. Chen, N. Pholchai, B. Reineke, P. W. H. Wong, E. Y. B. Pun, and S. Zhang, Continuous control of the nonlinearity phase for harmonic generations, Nat. Mater. **14**, 607 (2015).
[35] S. Campione, L. I. Basilio, L. K. Warne, and M. B. Sinclair, Tailoring dielectric resonator geometries for directional scattering and Huygens' metasurfaces, Opt. Express **23**, 2293 (2015).
[36] F. Aieta, M. A. Kats, P. Genevet, and F. Capasso, Multiwavelength achromatic metasurfaces by dispersive phase compensation, Science **347**, 1342 (2015).

[37] M. Khorasaninejad, A. Ambrosio, P. Kanhaiya, and F. Capasso, Broadband and chiral binary dielectric meta-holograms, Sci. Adv. **2**, e1501258 (2016).

[38] B. E. Saleh, M. C. Teich, and B. E. Saleh, *Fundamentals of Photonics* (Wiley, New York, 1991).

[39] H. S. Ee and R. Agarwal, Tunable metasurface and flat optical zoom lens on a stretchable substrate, Nano Lett. **16**, 2818 (2016).

[40] J. He, J. Ye, X. Wang, A. Kan, and Y. Zhang, A broadband terahertz ultrathin multi-focus lens, Sci. Rep. **6**, 28800 (2016).